

Modeling Microstructural Effects on Heterogeneous Temperature Fields within Polycrystalline Explosives

Nisha Mohan,^[a] Darby J. Luscher,^{*[b]} Marc J. Cawkwell,^[b] F. L. Addessio,^[b] and Kyle J. Ramos^[b]

Abstract: The paper addresses the role of crystal anisotropy on the evolution of heterogeneous temperature fields in plastic-bonded explosives (PBXs) under conditions of weak shock. The modeling approach is based on simplified idealizations of PBX microstructure including RDX grains and estane binder regions subjected to velocity boundary conditions representative of impact conditions in situ. The constitutive description of the microstructure constituents includes a dislocation-based, anisotropic, single crystal plasticity model for the explosive grains and a linear viscoelastic model to represent the estane binder. Large suites of simulations were used to systematically study the correla-

tion in heating of the grains with local wave dynamics, crystal orientation, and the microstructural neighborhood. These correlations were identified through the selection of characteristics of crystal anisotropy including oriented wave speeds and Taylor factor. A key observation is that the wave dispersion within a certain distance from the impact interface plays a dominant role in the temperature field. Beyond this distance, individual crystal orientations play a more dominant role, but cannot entirely account for the observed heterogeneity without consideration of the local microstructure neighborhood.

Keywords: energetic materials · mesoscale modeling · microstructure · finite element modeling · impact

1 Introduction

Impacts leading to weak shocks within plastic-bonded explosives (PBX) are associated with magnitudes of energy density that, if distributed homogeneously throughout the material, would cause temperatures insufficient to drive the rapid chemistry sometimes observed for these cases [1]. In such cases, heterogeneous thermomechanical interactions at the mesoscale (i.e. between the single-crystal and macroscale) lead to heterogeneously evolving temperature fields. Besides, it is known that the macroscopic response of the explosive can differ significantly depending on details of the microstructure and the thermomechanical response of its constituents [2–4]. Recent advances in theory and computational modeling of the thermomechanical response at microstructural scales suggest these tools may provide utility in improving our understanding of the relevant thermomechanical processes within explosive materials. For example, Barua et al. [5,6] have investigated the influence of binder decohesion on the dynamic thermomechanical response of statistical volume elements of PBX 9501. Keyhani et al. [7] expanded upon this framework in order to address the effects of the viscoplastic response within and frictional sliding between the energetic grains. Their simulations employed an isotropic model to represent the behavior of the energetic grains, thus the role of anisotropy was omitted from the assessment. Rai and Udaykumar [8] have performed mesoscale simulations of the dynamic response of explosives using an image-based technique to create models that explicitly resolve the interfaces between grains us-

ing a level set method. They also applied the framework to understand the effects of orientation of anisotropic voids during pore collapse within the material. That particular investigation did not include representation of the binder material. Chakravarthy and Gonthier [9] constructed mesoscale simulations within a framework including heat conduction to analyze the effects of metal particles on the temperature fields in shock consolidated binder-less explosives mixtures. A common aspect of each of these previous efforts is that they did not account for anisotropy in the thermomechanical response of individual grains, i.e. their models for the individual crystals were isotropic. Indeed, relatively little attention has been given to the role of crystal anisotropy in the context of heterogeneous temperature evolution in PBXs. LaBarbera and Zikry [10] and Wang et al. [11] have incorporated anisotropic single crystal models to represent the thermomechanical response of individual explosive grains within such mesoscale simulations, but did not focus their attention on the nature of the anisotropy in producing heterogeneous temperature fields. Barton et al. [12] and Austin et al. [13] have numerically investigated the temperature evolution and associated chemistry associated

[a] N. Mohan
ATCO SpaceLab
Calgary, AB T3E 8B4, Canada

[b] D. J. Luscher, M. J. Cawkwell, F. L. Addessio, K. J. Ramos
Los Alamos National Laboratory
Los Alamos, NM, USA
*e-mail: djl@lanl.gov

with the collapse of pores embedded within HMX crystals using an anisotropic single crystal model, but their investigation was not focused on PBXs in aggregate.

One key question pertaining to the thermomechanical response of PBXs under impact loading is the precise role of crystal anisotropy. It has been demonstrated that the behavior of individual crystals depends upon the orientation of the crystal lattice with respect to the impact direction [14–19]. Several models for the anisotropic shock response of individual molecular crystals have been developed for various materials, including HMX [12,19,20], PETN [21], and RDX [22–24]. Luscher et al. [23] developed a dislocation-based anisotropic model for the combined thermoelastic and plastic slip behavior of RDX crystals and demonstrated that it could capture the orientation dependence observed from plate impact experiments of Hooks et al. [16,25]. In light of the recognized importance of anisotropy and crystal orientation to the impact response of single crystals combined with the aforementioned mesoscale simulations of PBX response, a natural question emerges as to what extent does the anisotropy of crystals affect the temperature response of shocked, heterogeneous PBXs.

Here we seek to understand the role of crystal anisotropy within the context of simulations of PBX and to quantify these effects for an idealized microstructure description. The idealization comes in the form of the heterogeneity included in the microstructural description of the material. We consider only two sources, namely, the local anisotropy with different orientations within each crystal in the PBX and the presence of a binder. In order to explicitly resolve the binder region, we use idealized microstructures with a large proportion of binder phase in relation to many PBX formulations. To isolate and focus on the role of anisotropy, we do not include fracture, void collapse, frictional interactions, or any other source of heterogeneity within these idealized microstructures.

The organization of the paper is as follows. The modeling approach including microstructure geometry, computational mesh, constitutive models, and boundary conditions are described in Section 2. Section 3 is arranged into several parts to separately analyze and discuss the implications of wave dispersion, the relative role of microstructure neighborhood versus individual crystal orientation, and correlations between temperature fields and characteristics of crystal anisotropy. The main conclusions are summarized in Section 4.

2 Modeling Approach

In order to independently assess both the effect of the orientation of anisotropic single crystals and microstructure interactions on the heterogeneity of the resulting temperature fields under weak impacts, finite element simulations of both single crystals and idealized simple microstructure geometries were conducted using Abaqus/Explicit [26]. Our

idealized representation of PBX microstructure includes both an 85.6% area fraction of RDX grains and Estane binder. The heterogeneity is introduced by interactions of the individually oriented anisotropic grains and binder. To isolate and assess the role of crystal anisotropy in the evolution of mesoscale temperature fields, we omit many realistic aspects of PBX microstructure that are commonly anticipated to affect actual explosive materials. For example, we do not attempt to address pore collapse, inter- or intra-granular fracture and sliding, nor localized shear banding in this investigation.

2.1 Geometry and Computational Mesh

Simulations of the plane wave impact response of oriented single crystals were used to establish a baseline for comparisons with microstructure simulations. These single-crystal calculations are performed on a one-dimensional array of 280 three-dimensional elements (Abaqus C3D8R) along the length of $L = 1$ mm, as depicted in Figure 1.

The PBX microstructure geometry comprises a height $H = 1$ mm and length $L = 1$ mm with a characteristic grain size, $D_{gr} = 200$ μm which was synthesized by a Voronoi tessellation in two dimensions. The initial seeds are uniformly positioned within the specimen with a grid of spacing $\Delta H = D_{gr}$ and $\Delta L = (\sqrt{3}/2)D_{gr}$, respectively. Every other column of seeds was shifted vertically by $\Delta H/2$. This positioning of grain centers would lead to a uniform tessellation into hexagonal grains of identical size. The coordinates of seeds within the distance D_{gr} of the domain boundary remained unperturbed in order to preclude narrow slivers of grains at the boundary which would lead to unacceptably poor element geometry. The seed coordinates within the interior domain were randomly perturbed by

$$(\delta x, \delta y)_i = \frac{1}{4}(\Delta H^2 + \Delta L^2)^{1/2}(U_x, U_y)_i \quad (1)$$

where U_x and U_y are random real values sampled over a normal distribution for each seed, i . A Voronoi tessellation was then performed to compute the vertices and connectivity of grain geometry. The coordinates of each grain

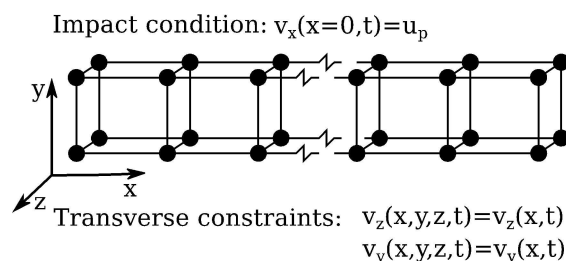


Figure 1. Schematic of the computational grid and initial/boundary conditions for single crystal impact simulations.

were scaled with respect to its center in order to create a final area fraction of grains of 85.6% and the region in between grains is treated as the binder material. The resulting geometry is illustrated in Figure 2. A discretization of the microstructure geometry into four-noded quadrilateral elements was computed using a two-dimensional paving algorithm in the finite element pre-processing software, Cubit [27]. Several discretizations, with the total number of elements ranging from 80,000 to 5×10^6 , were used to ensure reasonable accuracy in the extracted features discussed below.

2.2 Material Models

The anisotropic single crystal model and corresponding parameters developed by Luscher et al. [23] and the equation of state developed by Cawkwell et al. [28] were used to represent the constitutive behavior of the RDX in single-crystal and PBX simulations. This model is defined as a user subroutine, VUMAT, for calculations performed in Abaqus/Explicit. The temperature evolution under combined (weak) shock compression and plastic deformation is computed within the user-subroutine according to the rate-form algorithm from Luscher et al. [29]. Within the PBX calculations the orientation of each individual grain was randomly sampled from a uniform distribution over $SO(3)$. The orientations of these individual grains were also used for the suite of single-crystal calculations. In other words, a single-crystal calculation was performed for each grain orientation within the suite of PBX model calculations. In order to iso-

late the effects of crystal orientation on temperature fields, all material properties except the orientation are identical in each of the grains. The binder region represents the polymeric material, estane, and was modeled using a Maxwell linear viscoelastic constitutive behavior with the parameters identified by Mas et al. [30].

2.3 Initial and Boundary Conditions

Initial conditions consist of the initial temperature of $T_0 = 300$ K for all calculations and that all material points are initially at rest, i.e. $\mathbf{v}(\mathbf{X}, t=0) = 0$. The boundary conditions applied to the PBX and single-crystal simulations include a constant particle velocity of $v_x(x=0, t) = 600$ m/s applied at all nodes along the left boundary of the domain and held constant throughout simulation time. Within the PBX simulations, the component of velocity along \mathbf{e}_2 is restrained, i.e. $v_y(y=0, t) = v_y(y=H, t) = 0$.

Within the single-crystal calculations, constraint equations are applied to nodal displacements along the $y=0$, $y=h_{el}$, $z=0$, and $z=h_{el}$ surfaces to allow transverse components of the induced wave (cf. Luscher et al., [23]).

2.4 Nominal Simulation Results and Mesh Convergence

Simulation results for the case of a single crystal oriented such that the impact is on (210) planes at a particle velocity of $u_p = 600$ m/s lead to a final temperature and pressure of $T \approx 385$ K and $P \approx 4$ GPa, respectively. These conditions are at the incipient transformation from the α to γ solid phases in RDX, thus represented a maximum particle velocity leading to the highest temperature increase that could be considered without including the complexities of solid-solid phase transformations [24]. The element size used here, $h_{el} \approx 3.5$ μm is consistent with that employed by Luscher et al. [23]. A subset of calculations was repeated using a finer grid of $h_{el} \approx 2$ μm to verify that the selected resolution was sufficient for computing the temperature fields. The difference in temperatures was less than 0.5 K between the two grids. All results from single crystal calculations are reported at a final simulation time of $t = 0.3$ μs .

Contour plots of results from a selected PBX microstructure simulation at the simulation time $t = 0.3$ μs are shown in Figure 3. The temperature within the left-most column of grains was observed in all simulation cases to be systematically higher than in the interior region of the material domain. We attribute this to artificial wall heating associated with the instantaneous application of particle velocity at the left boundary. Because these temperatures are considered to be an artifact of hydrodynamic calculations, we omit the first column of grains from the analysis of simulation results in the following section. A visual comparison of the temperature and effective plastic strain fields are presented in Figures 3 and 4, respectively, which suggest a cor-

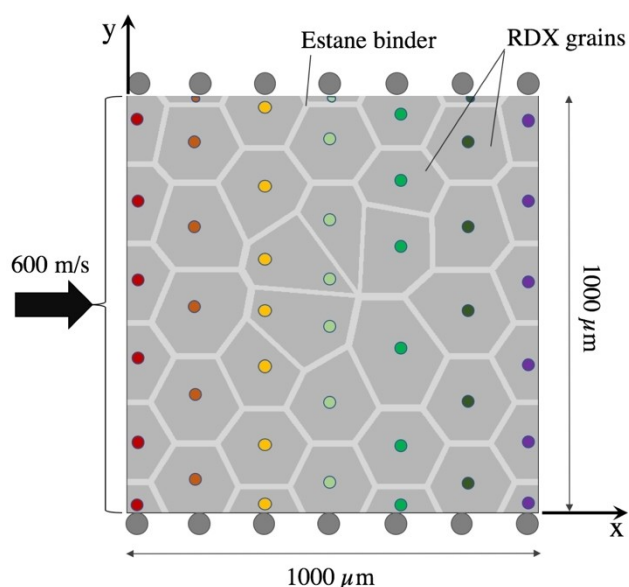


Figure 2. Schematic of the geometry for PBX models. The nominally 200 μm sized RDX grains are shaded dark gray and the binder material is light gray. The colored dots in the center of grains refer to the column-based grouping used for post-processing results.

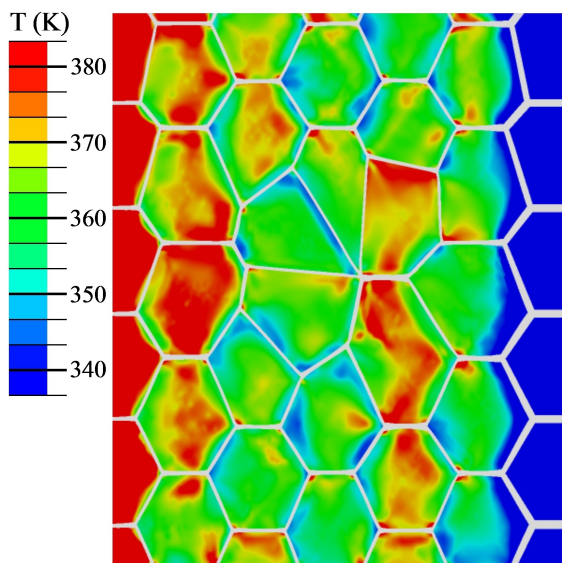


Figure 3. Contour plot of temperature field within microstructure. The incident compression wave is traveling from left to right and has nearly reached the right-most boundary of the microstructure.

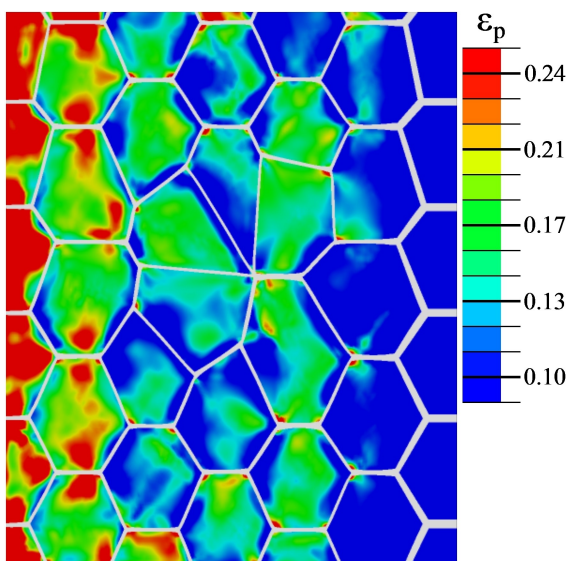


Figure 4. Contour plot of plastic strain field within microstructure. The incident compression wave is traveling from left to right and has nearly reached the right-most boundary of the microstructure.

relation between plastic strain and temperature. Variations of the temperature within each grain are also visible in Figure 3. Hotter regions and higher plastic strains within grains are found to arise at the grain corners and grain-binder interfaces. Also apparent in Figure 3, is a region of elevated temperature associated with a column of grains in the interior of the domain; this is not a systematic occurrence, instead of representing the particular combination of randomly selected grain orientations for one simulation case.

Fluctuations including both increases and decreases from the average grain temperature associated with the regions near crystal boundaries are attributed to local wave dynamics from the impedance differences across the interface between RDX and binder, as well as local stress concentrations due to the corners of the grains. Our observations are consistent with results from previous mesoscale simulations including approximately 1 GPa impacts using a single crystal plasticity model of RDX from LaBarbera and Zikry [10], and using a peridynamics representation of isotropic RDX behavior by Prakash and Seidel [31]. In these cases, heat transfer by conduction was included in the calculations.

The PBX microstructure simulations used to generate the results discussed in the subsequent section were conducted using a mesh with a nominal element size of 5 μm . This level of discretization was demonstrated to capture the average temperature within each grain with an acceptable level of accuracy (less than 3% error) by performing a mesh refinement study. Comparisons of the average temperature in each grain versus the element size are illustrated in Figure 5. From the mesh convergence study results, we observed that the peak temperature is not well resolved at these levels of mesh refinement. In order to accurately quantify peak temperatures in these types of microstructure calculations, we expect it would be necessary to include a coupled thermomechanical response with heat conduction and a very fine computational discretization. However, the average temperatures throughout a grain, spatial correlations in the temperature field, and area ratios of pronounced temperature values appear to be well resolved in these calculations using the nominal 5 μm element size. Consequently, the analysis of simulation results focuses on

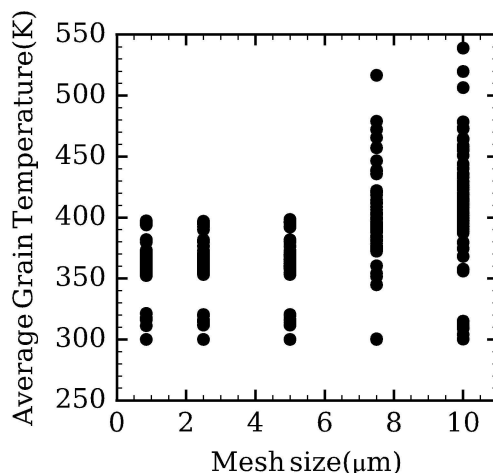


Figure 5. Results from mesh convergence study for PBX microstructure simulations. The average temperature in each grain is plotted versus the nominal element size for each of five finite element meshes. The simulations used to generate the results analyzed in detail in subsequent sections employ the computational mesh with a nominal element size of $h_{el} = 5 \mu\text{m}$.

metrics of the temperature field that are well resolved rather than peak temperature magnitudes.

3 Analysis of Simulation Results

A suite of 52 simulations of the PBX microstructure was performed, each with a different random sampling of the 42 distinctly oriented grains per simulation. The same initial microstructure geometry from Figure 2 was used for each of these simulations in order to emphasize the role of crystal anisotropy separately from grain geometry. Because the grains adjacent to the impact boundary condition were omitted from our analysis, this suite of calculations generated data for a total of 1,560 distinct crystallographic orientations. Additionally, a suite of single-crystal calculations was developed in which the temperature from impact on each of the 1,560 crystallographic orientations was separately computed

3.1 Evolution of Wave Structure Versus Shock Propagation Distance

The average temperature in each grain from the PBX simulations are plotted against the distance of that grain from the impact boundary in Figure 6. Clearly, the temperature rise is lower at further distances from the impact surface. This effect of decreasing temperature with increasing shock propagation distance was also observed at a similar impact velocity of 500 m/s, in the shock simulations of an HMX-based PBX of Wang et al. [11]. The relationship between the average grain temperature versus shock propagation dis-

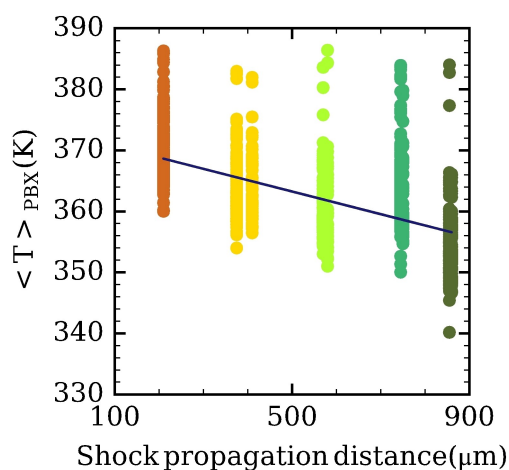


Figure 6. The average temperature in each grain versus the shock propagation distance for that grain from the impact, i.e. $X=0$, the boundary for 50 microstructure realizations employing 42 distinct crystal orientations. The color of the data point corresponds to the location of the grain in Figure 2 indicated by the same color. The gray dashed line is a visual aid for linear regression.

tance, apparent in this figure, is more appropriately understood in the context of wave dispersion due to the interaction of the wave with the heterogeneous microstructure as it transits through the material. To better demonstrate this phenomenon, the velocity-time history was averaged overall points of the same color in Figure 2. These averaged particle velocity-time histories are plotted in Figure 7 with each curve corresponding to the average from points of the same color in Figure 2. It is clear that the rise-time of the curves increases as the wave progresses through the microstructure. As the wave interacts with additional interfaces between grains of different orientations and binders, all of which have differing impedances along the propagation direction, the primary wave is complicated by small rarefactions and recompression waves. Collectively, these local wave dynamics lead to dispersion of the wavefront. The slope of the velocity-time history curve, i.e. the particle acceleration, is directly related to the strain rate of the material during its compression. Figure 8 illustrates the decrease in the particle acceleration computed as the slope of a line fit to the loading portion of velocity-time histories in Figure 7. Figure 9 shows the correlation between the average grain temperature and the particle acceleration rate, which seems to represent the actual phenomenon underlying the relationship between temperature and shock propagation distance (i.e. run distance) via wave dispersion.

Dick et al. [32] observed a similar wave dispersion response in plate impact experiments on PBX 9501, which comprises HMX rather than RDX crystals, and an estane binder. In particular, they observed that the rise-times in velocimetry traces for specimens of various thicknesses (i.e. shock propagation distance) increase throughout a certain distance and then stabilize into a steady wave. They observed that the shock propagation distance required for stabilization decreases with increasing shock strength. While a quantitative comparison between their ex-

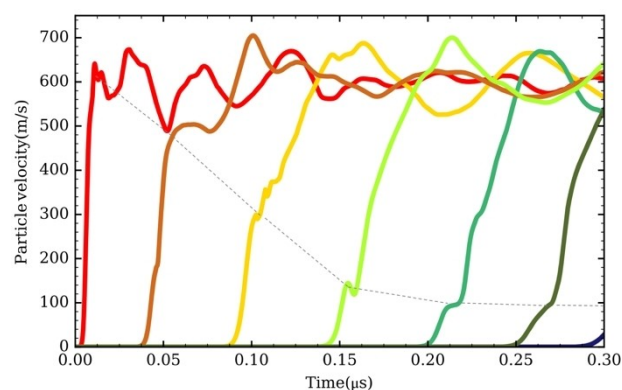


Figure 7. The evolution of velocity-time history as the wave transits through the microstructure. Each line in this plot corresponds to the average overall locations of the corresponding color in Figure 2. The results illustrate the wave dispersion associated with the heterogeneous interactions.

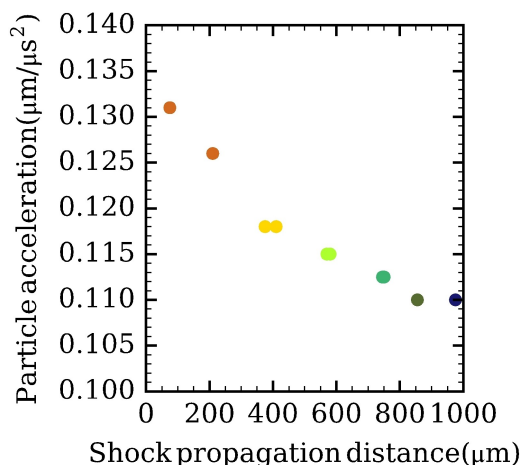


Figure 8. Plot of the nominal slope of the averaged velocity-time history at the wavefront, i.e. particle acceleration, versus shock propagation distance. The colors of data points in these plots correspond to the locations in Figure 2 indicated by the same color.

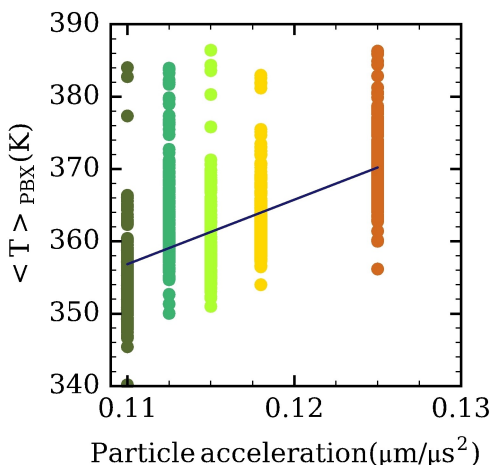


Figure 9. Plot of the apparent correlation of average grain temperature with the particle acceleration. The particle acceleration is used as a proxy for the strain rate during compression upon arrival of the incident wave. The colors of data points in these plots correspond to the locations in Figure 2 indicated by the same color.

perimental results and our simulation results is not meaningful because our simulations are for RDX, while their experiments were on HMX and at lower shock pressures, the trend is entirely consistent with what we see here and lends further credibility to our interpretation of these results.

While the results in Figure 8 are consistent with our explanation of a stabilization region in which the wave structure evolves, they depict model results for only a 1 mm simulation domain. Over this limited run distance, the demonstration of stabilization of the wave structure is arguably unsatisfactory. Therefore, we conducted a limited set of simulations using the same model approach with the domain extended to 2 mm in the shock direction to confirm

the stabilization of wave dispersion. The shock rates plotted in Figure 10 clearly exhibits stabilization at a run distance of 900 μm, where the shock rate converges to 0.11 μm/μs².

The correlation between temperature and shock propagation distance discussed above is only observed for wave run distances within this stabilization region (i.e. $X_1 < 900 \mu\text{m}$). The temperatures correlations with anisotropy factors were checked in the post-stabilization region ($\geq 900 \mu\text{m}$) with a limited number of tests. They were found to have same correlations as in the pre-stabilized region discussed before. This indicated that the temperature-anisotropy correlations were not affected by the shock-rates. This stabilization only affected the direct temperature-shock-rate correlations.

3.2 Microstructure Effects

By comparing the average temperature over each grain from the PBX simulations with the temperature obtained from a single crystal simulation of the same orientation, the influence of microstructure on the orientation dependence of heating from impact loading is further isolated. In Figure 11 the average temperature over a grain from the PBX simulations, i.e. $\langle T \rangle_{\text{PBX}}$, is plotted on the vertical axis against the corresponding single crystal temperature values, i.e. $\langle T \rangle_{\text{SC}}$, on the horizontal axis. If the microstructure had zero influence on the behavior of any individual grain, then these points would all lie along the gray dashed line. On the other hand, if the orientation of an individual grain had zero influence on the resulting temperature within the microstructure, then there would be no apparent correlation in Figure 11. Instead of either of these two limiting cases, the points are generally below the gray dashed line and there is a significant variance along the vertical axis.

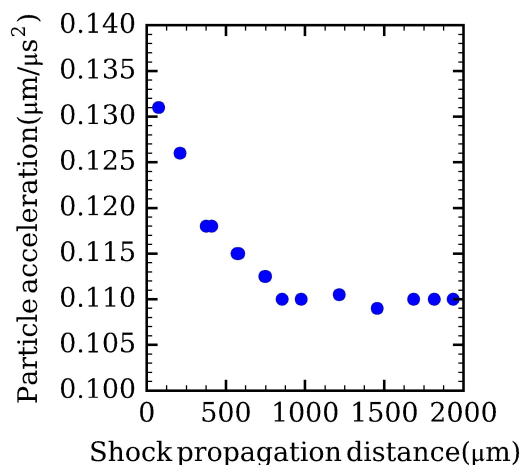


Figure 10. Particle acceleration rate plotted against shock propagation distance to demonstrate stabilization reached 900 μm.

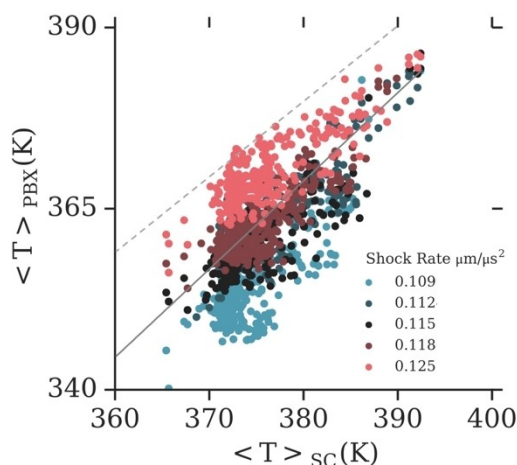


Figure 11. A comparison of temperatures from PBX microstructure simulations versus the temperature from the corresponding single crystal calculation. The orientation from each grain in each of the microstructure calculations was used for the single crystal simulations. The data points are colored based on the effective shock rate for that grain estimated as the slope of the particle velocity-time history. The dashed line corresponds to $\langle T \rangle_{PBX} = \langle T \rangle_{SC}$ and the solid line represents a linear regression between these data. The Spearman correlation coefficient for these data, $r_s = 0.68$, suggests that there is a strong correlation between the temperatures of a grain in the PBX simulations with that for impact on a single crystal with the same orientation.

The Spearman correlation coefficient, $-1 \leq r_s \leq 1$, is a statistical measure of the strength of a monotonic association between paired data. The Spearman correlation coefficient for these data, $r_s = 0.68$, suggests that there is a strong correlation between the temperatures of a grain in the PBX simulations with that for impact on a single crystal with the same orientation. That the temperatures in the PBXs are lower than their single-crystal counterparts is consistent with our assessment of wave dispersion. In other words, the impact response of single crystals does not exhibit the wave dispersion observed in the PBX and thus the single crystals are expected to respond with a higher particle acceleration (i.e. steeper shock front) and consequently higher temperature than in the PBX. Finally, the variance representing these microstructure effects appears to be smaller for the grains at the highest temperatures.

3.3 Correlation of Temperature with Wave Speed and Taylor Factor

From Figure 11 it is clear that the temperature evolution is affected by the orientation of individual grains due to their thermomechanical anisotropy. The sources of anisotropy within the single crystal model consist of both thermoelasticity (i.e. thermal expansion and elastic moduli) and plastic anisotropy attributed to the dislocation slip systems. It is plausible that the impedance differences associated

with the different alignments of the crystal lattice with respect to the dominant wave direction have an effect on the final Hugoniot state for a crystal. It is also plausible that particular crystallographic orientations are more or less favorable to accommodate the deformation via plastic slip. In this latter case, it could be expected that grains oriented more favorably for a plastic slip would result in more plastic work and higher temperatures.

The nominal quasi-longitudinal wave speeds for each crystal orientation were computed by solving the Christoffel equation, i.e. $(\rho C^2 \mathbf{I} - \mathbf{n} \cdot \mathbf{C} \cdot \mathbf{n}) \cdot \mathbf{u} = \mathbf{0}$, for the wave speed corresponding to the polarization vector, \mathbf{u} , whose component is most aligned along the main wave propagation direction, \mathbf{n} . The resulting wave speeds, C , range from 3.09 km/s to 3.70 km/s. The single crystal temperatures are plotted versus the quasi-longitudinal wave speed, C , in Figure 12 along with a linear regression. The Spearman coefficient, used as an indicator of the significance of a monotonic correlation between the variables, is 0.56 which suggests a strong positive correlation. Thus, there is a clear relationship between the orientation of an individual crystal and its post-impact response via the quasi-longitudinal wave speed of that crystal. Figure 13 compares the average temperature for each grain from the PBX simulations with the corresponding single crystal temperature as in Figure 11, but the data points are colored based on the value of the quasi-longitudinal wave speed for each particular crystal orientation. It is evident that there is not as strong of a correlation of the average grain temperature from PBX simulations with the quasi-longitudinal wave speed (as observed for the single crystal temperatures). Thus, the microstructure interactions diminish the observed correlation between single crystal temperatures and dynamic impedance.

This plot compares temperatures from the PBX microstructure simulations versus the temperature from the cor-

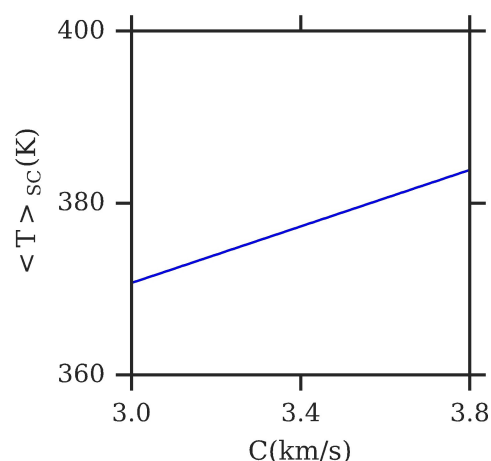


Figure 12. The correlation between the temperatures from single-crystal calculations and the quasi-longitudinal wave speed. The Spearman correlation coefficient for the linear regression is 0.56 suggesting a strong positive correlation.

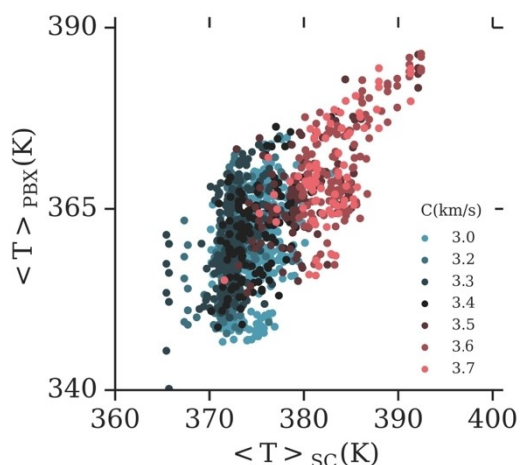


Figure 13. The relationship between post-impact temperatures and the quasi-longitudinal wave speeds.

responding single crystal calculation similar to Figure 11, except that here the data points are colored based on the quasi-longitudinal wave speed for each crystal orientation.

The Taylor factor, $M = \frac{\Sigma \Delta \gamma^a}{\Delta \epsilon_{11}} = \frac{\sigma_{11}}{\tau_{cr}}$, is an indicator of the amount of plastic work required in order to accommodate an imposed increment of axial plastic deformation, $\Delta \epsilon_{11}$. Taylor [33] proposed the metric as a means of identifying the subset of slip systems most likely to be activated to accommodate an imposed deformation, i.e. the set of slip systems providing the smallest value of M would require the least amount of work and thus represents the active subset of slip systems. Lieberman et al. [34] and Nguyen et al. [35] used the Taylor factor as a metric to characterize the anisotropy of plasticity in studying the likelihood for nucleation of damage at grain boundaries in polycrystalline materials. For the rate-dependent single-crystal model, we instead use the Taylor factor as an indicator of preferred crystal orientations for accommodating an imposed uniaxial deformation via plasticity; larger values of M indicate more plastic work, and thus more dissipative heating, are required to accommodate an imposed uniaxial deformation. We compute the Taylor factor from the contributions of all possible slip systems for a simplified rate-dependent viscoplastic expression of slip rates using the method outlined by Przybyla et al. [36], in which we assume all of the deformations are accommodated by plastic slip and the slip resistances on each slip system are identical. An inverse pole figure of the Taylor factor calculated in this manner over the domain of unique crystallographic orientations for RDX (orthorhombic symmetry) is shown in Figure 14.

The post-impact temperature from single-crystal calculations is plotted versus the Taylor factor in Figure 15 along with a line representing a linear regression. The Spearman correlation coefficient computed for these results is $r_s = 0.65$ indicating a strong likelihood of positive correlation con-

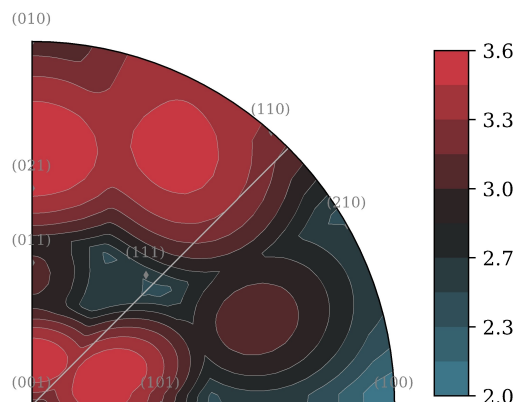


Figure 14. An inverse pole figure of the Taylor factors associated with various crystallographic orientations computed for RDX under an imposed uniaxial deformation. The lowest Taylor factor is associated with (100) orientation suggesting that the least amount of plastic work is required to accommodate a uniaxial deformation normal to RDX (100) planes.

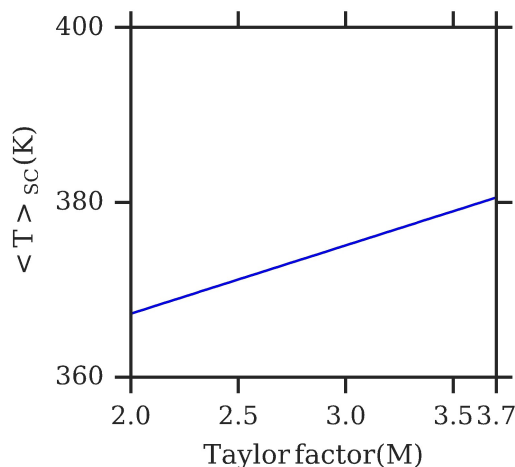


Figure 15. Temperature values from single-crystal calculations plotted versus Taylor factor. The linear regression line is associated with a Spearman correlation coefficient of 0.65 indicating a strong likelihood of positive correlation.

sistent with that expected, i.e. larger values of M are associated with more plastic work, and hence, higher post-impact temperatures. Figure 16 shows that the orientations with the largest values of the Taylor factor exhibit the least variance in temperature from the microstructure, and again, that the variance introduced by the microstructure because of the increase in wave dispersion with shock propagation distance diminishes the strength of correlation between Taylor factor and average grain temperature within the PBX.

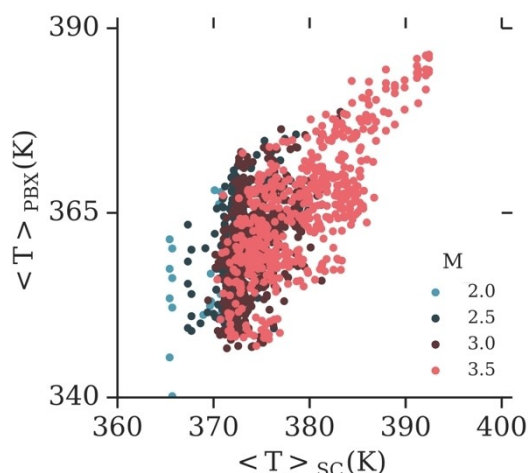


Figure 16. A comparison of temperatures from PBX microstructure simulations versus the temperature from the corresponding single crystal calculation. The plot is similar to Figure 11, except that here the data points are colored based on the Taylor factor for each crystal orientation. The Taylor factors computed for RDX are shown on an inverse pole figure in Figure 14 for reference.

4 Summary and Conclusion

The objective of the present investigation was to develop an improved understanding of the role of crystal anisotropy within the mesoscale thermomechanical response of PBXs. Toward this goal, we performed a suite of calculations designed to isolate effects associated with crystal orientation, wave dispersion, and the microstructural neighborhood in the vicinity of a crystal. The approach included two types of simulations, namely, simulations of microstructure response based on an idealized representation of a PBX, and calculations of single-crystal response to identical impact conditions. This approach enabled a comparison between the post-shock temperature within a single crystal and the corresponding temperature observed for a crystal of the same orientation within the microstructure. In consideration of over 1500 crystal orientations sampled within this framework, the comparison provides a statistical basis to isolate the roles of crystal anisotropy, e.g. as observed in single crystal experiments, from the effects of wave dispersion and the cumulative interactions of grains and binder within the microstructure. From this study, we draw several conclusions.

Consistent with experimental observations [32], there is a propagation distance within the PBX in which the heterogeneity in the microstructure perturbs the main shock wave with local wave dynamics associated with small rarefactions and recompressions. The shock propagation distance at which the wave stabilizes depends upon the impact velocity and was observed to be on the order of 900 μm in our calculations for a grain size of 200 μm and area fraction of 85.6% RDX crystals at a particle velocity of 600 m/s. Within this wave stabilization region, the rise-time or particle accel-

eration of the waves and correspondingly the strain rate is continually reduced. The simulation results show a strong correlation between the particle acceleration rate and the average temperature within the crystals. Hence, there is an apparent relationship between shock propagation distance and the decrease in mean crystal temperature within the stabilization region.

The post-shock temperature of individual crystals is dependent upon the orientation of the crystal with respect to the shock propagation direction. In particular, there is a strong correlation between the post-shock temperature and the quasi-longitudinal wave speed for the particular orientation, as well as the Taylor factor. Thus, anisotropic elasticity and anisotropic crystalline slip can, in part, explain the observed orientation dependence of shock temperatures.

The mean temperature of a particular grain within the microstructure is correlated to the temperature of a homogeneous single crystal with that same orientation. However, the mean temperatures of grains within the microstructure are generally lower than their single-crystal counterparts. This is because impacted single crystals do not exhibit the wave dispersion observed within the microstructure and represent a “microstructure neighborhood” effect. The microstructure effect is reduced for grains oriented in a direction preferential to higher temperatures.

Overall, the fluctuations in grain-averaged temperatures are on the order of 20% of the total temperature increase for the impact conditions considered, suggesting that crystal anisotropy can contribute a non-negligible component of the mesoscale response of PBXs. The present investigation motivates several follow on questions and, consequently, can serve as a jumping-off point for future investigations. We envision that the systematic incorporation of additional mechanisms, e.g. cohesive debonding, frictional sliding, pore collapse, will provide a useful framework for understanding the coupled mesoscale interactions that can affect explosive behavior, and perhaps, be exploited for the design of new, safer explosives.

Acknowledgements

This work was supported by the US Department of Energy through the Los Alamos National Laboratory. Los Alamos National Laboratory is operated by Triad National Security, LLC, for the National Nuclear Security Administration of U.S. Department of Energy (Contract No. 89233218CNA000001). In particular, the authors are grateful for the support of the Laboratory-Directed Research and Development program through the project 20180100DR (Boom or Bust? Predicting Explosive Safety Under Impacts).

Data Availability Statement

The data that support the findings of this study are available from the corresponding author upon reasonable request.

References

- [1] F. P. Bowden, A. D. Yoffe, Initiation, and Growth of Explosion in Liquids and Solids. **1952**, Cambridge University Press.
- [2] H. Moulard, J. W. Kerry, A. Delcios, The effect of RDX particle size on the shock sensitivity of cast PBX formulations. *8th International Detonation Symposium*, Albuquerque, NM, USA, July 15–19, **1985**, p. 902.
- [3] A. E. D. M. van der Heijden, R. H. B. Bouma, A. C. van den Steen, Physicochemical properties of nitramines influencing shock sensitivity. *Propellants Explos. Pyrotech.* **2004**, *29*, 304.
- [4] R. W. Doherty, D. S. Watt, Relationship between RDX properties and sensitivity. *Propellants Explos. Pyrotech.* **2008**, *33*, 4.
- [5] A. Barua, M. Zhou, A Lagrangian framework for analyzing microstructural level response of polymer bonded explosives. *Modell. Simul. Mater. Sci. Eng.* **2011**, *19*, 055001.
- [6] A. Barua, Y. Horie, M. Zhou, Energy localization in HMX estane polymer bonded explosives during impact loading. *J. Appl. Phys.* **2012**, *111*, 054902.
- [7] A. Keyhani, S. Kim, Y. Horie, M. Zhou, Energy dissipation in polymer-bonded explosives with various levels of constituent plasticity and internal friction. *Comp. Mat. Sci.* **2019**, *159*, 136–149.
- [8] N. K. Rai, H. Udaykumar, Mesoscale simulation of reactive pressed energetic materials under shock loading. *J. Appl. Phys.* **2015**, *118*, 245905.
- [9] S. Chakravarthy, K. A. Gonthier, Analysis of microstructure-dependent shock dissipation and hot-spot formation in granular metalized explosive. *J. Appl. Phys.* **2016**, *120*, 024901.
- [10] D. LaBarbera, M. Zikry, Heterogeneous thermo-mechanical behavior and hot spot formation in RDX-estane energetic aggregates. *Int. J. Solids Struct.* **2015a**, *62*, 91–103.
- [11] X. Wang, Y. Wu, F. Huang, T. Jiao, R. J. Clifton, Mesoscale thermal-mechanical analysis of impacted granular and polymer-bonded explosives. *Mech. Mater.* **2016**, *99*, 68–78.
- [12] N. R. Barton, N. W. Winter, J. E. Reaugh, Defect evolution and pore collapse in crystalline energetic materials. *Modell. Simul. Mater. Sci. Eng.* **2009**, *17*, 035003.
- [13] R. A. Austin, N. R. Barton, J. E. Reaugh, L. E. Fried, Direct numerical simulation of shear localization and decomposition reactions in shock-loaded HMX crystal. *J. Appl. Phys.* **2015**, *117*, 185902.
- [14] J. Dick, Effect of crystal orientation on shock initiation sensitivity of pentaerythritol tetranitrate explosive. *Appl. Phys. Lett.* **1984**, *44*, 859–861.
- [15] J. Dick, J. Ritchie, Molecular mechanics modeling of shear and the crystal orientation dependence of the elastic precursor shock strength in pentaerythritol tetranitrate. *J. Appl. Phys.* **1994**, *76*, 2726–2737.
- [16] D. E. Hooks, K. J. Ramos, A. R. Martinez, Elastic-plastic shock wave profiles in oriented single crystals of cyclotrimethylene trinitramine (RDX) at 2.25 GPa. *J. Appl. Phys.* **2006**, *100*, 024908.
- [17] K. J. Ramos, D. E. Hooks, T. D. Sewell, M. J. Cawkwell, Anomalous hardening under shock compression in (021)-oriented cyclotrimethylene trinitramine single crystals. *J. Appl. Phys.* **2010**, *108*, 066105.
- [18] K. J. Ramos, M. J. Cawkwell, C. A. Bolme, D. E. Hooks, Effects of orientation, pressure/strain rate, and microstructure on the quasi-static deformation and shock response of single-crystal explosives. *15th Symposium (International) on Detonation*, San Francisco, CA, USA, July 13–18, **2014**, p. 1562–1572.
- [19] N. Grilli, M. Koslowski, The effect of crystal orientation on shock loading of single crystal energetic materials. *Comp. Mat. Sci.* **2018**, *155*, 235–245.
- [20] N. Grilli, M. Koslowski, The effect of crystal anisotropy and plastic response on the dynamic fracture of energetic materials. *J. Appl. Phys.* **2019**, *126* (15), p.155101.
- [21] J. M. Winey, Y. M. Gupta, Anisotropic material model and wave propagation simulations for shocked pentaerythritol tetranitrate single crystals. *J. Appl. Phys.* **2010**, *107*, 103505.
- [22] S. De, A. R. Zamiri, Rahul, A fully anisotropic single crystal model for high strain rate loading conditions with an application to α -RDX. *J. Mech. Phys. Solids*. **2014**, *64*, 287–301.
- [23] D. J. Luscher, F. L. Addessio, M. J. Cawkwell, K. J. Ramos, A dislocation density-based continuum model of the anisotropic shock response of single-crystal cyclotrimethylene trinitramine. *J. Mech. Phys. Solids* **2017**, *98*, 63–86.
- [24] F. L. Addessio, D. J. Luscher, M. J. Cawkwell, K. J. Ramos, A single-crystal model for the high-strain rate deformation of cyclotrimethylene trinitramine including phase transformations and plastic slip. *J. Appl. Phys.* **2017**, *121*, 185902.
- [25] D. E. Hooks, K. J. Ramos, A. R. Martinez, Erratum: "Elastic-plastic shock wave profiles in oriented single crystals of cyclotrimethylene trinitramine (RDX) at 2.25 GPa" *J. Appl. Phys.* **2006**, *100*, 024908. *J. Appl. Phys.* **2011**, *109*, 089901.
- [26] Abaqus v6.12, 2012. Abaqus Theory and Analysis Manual. Dassault Systemes Simulia Corp., Providence, RI, USA.
- [27] Cubit (Software), **2016**. Sandia National Laboratories.
- [28] M. J. Cawkwell, D. J. Luscher, F. L. Addessio, K. J. Ramos, Equations of state for the α and γ polymorphs of cyclotrimethylene trinitramine. *J. Appl. Phys.* **2016**, *119*.
- [29] D. J. Luscher, M. A. Buechler, D. J. Walters, C. A. Bolme, K. J. Ramos, On computing the evolution of temperature for materials under dynamic loading. *Int. J. Plast.* **2018**, *111*, 188–210.
- [30] E. Mas, B. Clements, B. Blumenthal, C. Cady, G. Gray III, C. Liu, A viscoelastic model for PBX binders *AIP Conf. Proc.* **2002**, *661*–664.
- [31] N. Prakash, G. D. Seidel, Effects of microscale damage evolution on piezoresistive sensing in nanocomposite bonded explosives under dynamic loading via electromechanical peridynamics. *Modell. Simul. Mater. Sci. Eng.* **2017**, *26*, 015003.
- [32] J. J. Dick, A. R. Martinez, R. S. Hixson, Plane impact response of PBX 9501 below 2 GPa. Technical Report LA-13426-MS **1998**, Los Alamos National Laboratory.
- [33] G. I. Taylor, Plastic strain in metals. *J. Inst. Met.* **1938**, *62*, 307–324.
- [34] E. J. Lieberman, R. A. Lebensohn, D. B. Menasche, C. A. Bronkhorst, A. D. Rollett, Microstructural effects on damage evolution in shocked copper polycrystals. *Acta Mater.* **2016**, *116*, 270–280.
- [35] T. Nguyen, D. J. Luscher, J. W. Wilkerson, The role of elastic and plastic anisotropy in intergranular spall failure. *Acta Mater.* **2019**, *168*, 1–12.
- [36] C. P. Przybyla, B. L. Adams, M. P. Miles, Methodology for determining the variance of the Taylor factor: application in Fe-3% Si. *J. Eng. Mater. Technol.* **2007**, *129*, 82–93.

Manuscript received: October 23, 2020

Revised manuscript received: January 13, 2021

Version of record online: February 16, 2021